Morphology, age and sediment dynamics of the upper headwall of the Sahara Slide Complex, Northwest Africa: Evidence for a large Late Holocene failure

Wei Li[a]*, Tiago M. Alves[b], Morelia Urlaub[c], Aggeliki Georgiopoulou[d], Ingo Klaucke[c], Russell B. Wynn[e], Felix Gross[a], Mathias Meyer[c], Janne Repschläger[a], Christian Berndt[c], Sebastian Krastel[a]

[a] Institute of Geosciences, University of Kiel, Kiel 24118, Germany
[b] 3D Seismic Lab, School of Earth and Ocean Sciences, Cardiff University, Main Building, Park Place, Cardiff, CF10 3AT, United Kingdom
[c] GEOMAR Helmholtz Centre for Ocean Research Kiel, 24148 Kiel, Germany
[d] UCD School of Earth Sciences, University College Dublin, Belfield, Dublin 4, Ireland
[e] National Oceanography Centre, European Way, Southampton, Hampshire SO14 3ZH, United Kingdom
*Correspondence to: Wei Li (li@geophysik.uni-kiel.de)

Abstract

The Sahara Slide Complex in Northwest Africa is a giant submarine landslide with an estimated run-out length of ~ 900 km. We present newly acquired high-resolution multibeam bathymetry, sidescan sonar, and sub-bottom profiler data to investigate the seafloor morphology, sediment dynamics and the timing of formation of the upper headwall area of the Sahara Slide Complex. The data reveal a ~35 km-wide upper headwall opening towards the northwest with multiple slide scarps, glide planes, plateaus, lobes, slide blocks and slide debris. The slide scarps in the study area are formed by retrogressive failure events, which resulted in two types of mass movements, translational sliding and spreading. Three different glide planes (GP I, II, and III) can be distinguished approximately 100 m, 50 m and 20 m below the seafloor. These glide planes are widespread and suggest failure along pronounced, continuous weak layers. Our new data suggest an age of only about 2 ka for the failure of the upper headwall area, a date much younger than derived for the landslide deposits on the lower reaches of the Sahara Slide Complex, which are dated at 50-60 ka. The young age of the failure contradicts the postulate of a stable slope off Northwest Africa during times of relative stable sea-level highstands. Such an observation suggests that submarine-landslide risk along the continental margin of Northwest Africa should be reassessed based on a robust dating of proximal and distal slope failures.

Keywords: Submarine landslide evolution; multiple slope failure; weak layers; slope instability; geohazards.

1. Introduction

Submarine landslides are a widespread phenomenon documented in multiple geological settings such as tectonically active margins, passive continental margins and volcanic islands (Masson et al., 2006; Moernaut and De Batist, 2011; Krastel et al., 2014; Lamarche et al., 2016). Submarine landslides transport large volumes of sediments into deeper continental slope and abyssal areas, and some present sufficient density and speed to pose important hazards to anthropogenic structures in shallower water (Lo Iacono et al., 2012). Submarine landslides have in the past generated tsunamis causing widespread damage to coastal communities (Harbitz et al., 2014). In addition, turbidity currents generated by submarine landslides are one of the most important near-seafloor geohazards, as they can potentially damage deep-water equipment and engineering infrastructure such as pipelines and communication lines (Piper and Aksu, 1987; Masson et al., 2006; Talling et al., 2014). Hence, the recognition of submarine landslides on continental margins is important to: a) the recognition of areas prone to slope instability on modern continental slopes, b) the investigation of possible triggers of slope instability, and c) the investigation of the global causes of submarine landsliding such as eustasy, tectonics, and climatic events (Vanneste et al., 2014). Other factors that have been proposed to trigger submarine landslides at a local scale include high sedimentation rates (Leynaud et al., 2007; Li et al., 2014), excess pore pressure (Berndt et al., 2012), gas hydrate dissociation (Sultan et al., 2004) and earthquakes (Sultan et al., 2004; Zhao et al., 2015).

In Northwest Africa, multiple large-scale submarine landslides have occurred during the Quaternary (Krastel et al. 2012). The most prominent submarine landslides in the region include the Sahara Slide Complex (Embley, 1982; Gee et al., 1999; Georgiopoulou et al., 2010), the Mauritania Slide Complex (Antobreh and Krastel, 2007; Henrich et al. 2008; Förster et al. 2010), the Cap Blanc Slide (Krastel et al., 2006) and the Dakar Slide (Meyer et al., 2012). The Sahara Slide Complex is one of the largest known submarine slides in the world, and affected an area of 48,000 km^2 of the Northwest African Margin (Embley et al., 1982; Fig. 1). During a period of rapid sea-level rise at ~50-60 ka, high primary productivity in surface waters offshore Northwest Africa resulted in the accumulation of fine-grained pelagic/hemipelagic sediment on the continental slope (Bertrand et al., 1996; Krastel et al., 2006). Multiple slide events were interpreted to have occurred retrogressively at this time (Georgiopoulou et al., 2007; 2009). As a result, the Sahara Slide Complex remobilised ~600 km^3 of sediments along a distance of ~900 km (Georgiopoulou et al., 2010). The slide eroded and entrained a volcaniclastic layer when passing close to the Canary Islands, generating a two-phase debris flow; a lower volcaniclastic debris-flow phase and an upper pelagic debrite (Gee et al., 1999; Georgiopoulou et al, 2010). The long runout-distance of the flow was explained by retaining excess pore pressure in the lower

volcaniclastic debris flow phase, which acted as a lubricating carpet for the overlying relatively impermeable pelagic debris flow phase (Gee et al., 1999; Georgiopoulou et al., 2010).

Most of the published geological information on the Sahara Slide Complex has been acquired in its distal depositional part (Gee et al., 1999; 2001; Georgiopoulou et al., 2009; 2010). However, limited attention has been paid to its headwall, chiefly due to the lack of high-quality data on the upper continental slope of Northwest Africa. Reconnaissance data show that the Sahara Slide Complex is marked by the presence of two major scarps (named lower and upper headwall scarps), each up to 100 m high (Fig. 2). Sparse seismic lines suggested stacked landslide deposits (Georgiopoulou et al., 2010; Krastel et al., 2012).

In this manuscript, we present a combination of new high-resolution multibeam bathymetry, sidescan sonar, sub-bottom profiler, and sediment gravity-core data from the upper headwall of the Sahara Slide Complex. This manuscript presents the first detailed morphological analysis of the upper headwall of the Sahara Slide Complex, so we:

a) Determine the distribution, relative timing and estimated volumes of the different slide events in order to reconstruct the evolution of the upper headwall;

b) Analyse the different types of mass movements that occurred in the investigated area;

c) Discuss the timing of slope failures;

d) Assess the hazards related to the failure of the upper headwall.

The study contributes to the wider discussion about the stability of continental margins during the present-day relative sea-level high stand (e.g., Owen et al., 2007; Lee; 2009; Smith et al., 2013). We show that it is crucial to investigate both landslide deposits and the failure area in order to reconstruct the evolution of submarine slide complexes.

2. Geological setting

The Northwest African continental margin is one of the best-studied passive margins in the world. On this margin, earthquakes of magnitude $M \geq 7$ have rarely been recorded away from the Gulf of Cadiz (Seibold, 1982), but moderate earthquakes ($4 \leq M \leq 6$) are commonly observed in association with the reactivation of old weakness zones created during the opening of the Atlantic Ocean (Hayes and Rabinowitz, 1975; Pereira and Alves, 2011). The width of the continental shelf of Northwest Africa is generally 40-60 km, reaching a maximum width of more than 100 km offshore Western Sahara (Fig. 1). The shelf break is observed at a water depth between 100 m and 200 m (Fig. 1; Wynn et al., 2000). The continental slope dips 1° to 6° from a depth of 200 to 1500 metres, while the continental rise is less than 1° beyond a depth of 4000 m. The Northwest African continental margin has been affected by complex sediment transport processes since its inception (Wynn et al., 2000; Krastel et al., 2012).

Most of the continental margin of Northwest Africa is now arid and records limited sediment supply by rivers, even during past glacial times (Weaver et al., 2000; Wynn et al., 2000). The margin is affected by both a seasonal and permanent oceanic upwelling system (Lange et al., 1998). Upwelling and associated high organic productivity are concentrated along the outer shelf and upper slope regions, resulting in sedimentation rates of 5 cm/ka on average, which increased to 16.5 cm/ka during the last glacial period (Bertrand et al., 1996; Weaver et al. 2000). Deep-water hemipelagic sedimentation in Northwest Africa typically consists of silts, muds, carbonate-rich marls and oozes (Weaver and Kuijpers, 1983). Wind-blown sediments transported from the Sahara Desert provide additional terrigenous sediment supply to the Northwest African continental margin (Holz et al., 2004; Henrich et al., 2008).

3. Data and methods

The dataset used in this study consists of deep-towed sidescan sonar, multibeam bathymetry and gravity cores collected at the upper headwall of the Sahara Slide Complex (Fig. 2a). Sub-bottom profiler data mounted on the sidescan sonar and a hull-mounted Parasound system were also interpreted in this work.

3.1 Acoustic data

The bulk of multibeam bathymetric data were collected during Cruise MSM11/2 (Bickert and cruise participants, 2011) using a hull-mounted Kongsberg Simrad system EM120. The nominal sonar frequency of this system is 12 kHz with an angular coverage sector of up to 150°. A total of 191 beams were recorded for each ping. The data were gridded at 50 m; vertical resolution is in the range of 5 -10 m. Sidescan sonar data were acquired during Cruise P395 using an EdgeTech DTS-1 sonar (Krastel and cruise participants, 2011). This sidescan sonar system was towed around 100 m above the seafloor and it worked with an operating frequency centered at 75 kHz; swath range per side was 750 m. The 75 kHz signal has a bandwidth of 7.5 kHz with a pulse length of 14 ms. Horizontal resolution after processing is 1 m, which enables the identification of complex morphological and sedimentary features based on the observed variations in backscatter (Golbeck, 2010).

Deep-towed sub-bottom profiler data were collected with the sidescan sonar mosaic during cruise P395. The profiler operated with chirp based frequencies ranging from 2 kHz and 10 kHz, for a 20 ms pulse length. These frequencies provide a penetration depth of up to 30 m and a vertical resolution of a few decimeters (Golbeck, 2010). Parasound sub-bottom seismic profiles acquired during RV Meteor M58/1 and RV Maria S. Merian MSM11/2 expeditions complete the geophysical dataset utilised in this work. The Parasound system DS3 (Atlas Hydrographic®) is a hull-mounted parametric sub-bottom profiler with an opening angle of only 4°. The selected frequency was 4 kHz, providing a sub-meter vertical resolution for strata below the seafloor.

3.2 Gravity cores and dating

Sediment cores were collected in the upper headwall of the Sahara Slide by utilising a standard gravity corer equipped with a 5-m barrel. In total, 10 gravity cores were acquired in the upper headwall, nine (9) from the landslide area and one (1) from undisturbed sediments above the headwall area (Fig. 2a). A sample for dating the undisturbed drape on top of landslide deposits was taken from Core P395-07-1 (24°27,36' N, 17°08,18' W) collected at a water depth of 2132 m (Figs. 2a). The sample was taken 3 cm below the seafloor (bsf), which is the interval of the first hemipelagites that drape the debris deposits. No other cores included sufficient undisturbed sediment drape for dating on top of the landslide deposits. Remnants of brownish Holocene sediments were found in a few core liners, suggesting that some undisturbed sediment drape was lost during core recovery, but we do not have any indication of a loss of more than 10 cm of surface sediments. As we were not able to date the Holocene drape in any other gravity core, we took an additional sample from Core P395-04-1 (24°14,70' N, 17°13,40' W) for our datings. Core P395-04-01 was collected at a water depth of 1930 m (Fig. 2a). The sample in the core was taken in 5 cm bsf in a clast remobilized together with the slide deposits. Hence this sample provides a maximum age of the failure.

Accelerated Mass Spectrometry (AMS) ^{14}C-age dating was applied on monospecific samples of the planktonic foraminifera *Globigerinoides ruber* (w) and it was carried out by the ^{14}C-age Leibniz-Laboratory of Kiel University, Germany. The conventional ^{14}C age was calculated according to Stuiver and Polach (1977) method. A δ^{13}C correction for isotopic fractionation was applied to the method based on the ^{13}C/^{12}C ratio measured by the AMS-system simultaneously with the ^{14}C/^{12}C ratio. The Calib 7.1 software, in combination with the Marine13 calibration curve, was used to calibrate the radiocarbon age (Stuiver and Reimer, 1986; Reimer et al. 2013). A reservoir age of ±500 years was assumed for the calibration of the radiocarbon age (e.g., Mangerud and Gulliksen, 1975).

To estimate the age of the Sahara Slide we follow the method in Urlaub et al. (2013). We consider the location of the sample to date (vertical distance to the top of the landslide) as the main uncertainty in our analyses, and we do not take into account the measurement error of the ^{14}C AMS method. The sample in Core P395-07-1 was obtained very close (1 cm above) to the slide deposits, i.e. comprising the first 'background' hemipelagites deposited after the slide event. The age of the slide is calculated as the radiocarbon age of the sample + D_{sf}/SR, where D_{sf} is the distance from the sample location to the upper surface of the slide deposit, and SR is the sedimentation rate (Urlaub et al., 2013).

4. Results

The failure area of the Sahara Slide Complex consists of two major headwalls, which are called lower and upper headwalls in the following sections. Each of the headwall scarps has height of about 100 m (Fig. 2b). The upper headwall is found at a water depth of about 2000 m, while the lower headwall is located ~50 km downslope at a water depths of ~2700 m. In this paper we focus on the upper headwall, as only sparse data are available from the lower headwall.

4.1 Morphology of the upper headwall

The upper headwall of the Sahara Slide Complex has an average width of ~35 km and is U-shaped, facing the northwest (Fig. 2a). Several morphological features, including slide scarps, glide planes, plateaus, slide lobes and slide blocks can be identified on the acoustic data (Figs. 2 to 5). In the following sub-sections, we will describe the morphology of the main seafloor features.

4.1.1 Slide scarps

The bathymetric data show significant sediment evacuation from the Sahara Slide Complex's headwall, with well-exposed scarps (Figs. 3a and 3b). The upper headwall is located at water depths between 1800 m and 2100 m, where slope gradients range from 4° to 23° (Fig. 2a). The height of the headwall scarps ranges from 20 m to 100 m. Two sidewall scarps show a SE-NW direction. Sidewall scarps are steep with gradients of 7°-18° and have heights of 47 m to 86 m, cutting into stratified deposits (Figs. 2a, 4b and 5b).

4.1.2 Glide planes

Three glide planes rooted at different stratigraphic depths, but all parallel to stratigraphy, are observed on both bathymetric and Parasound data (Figs. 3a, b and 4b). These glide planes, GP I, GP II and GP III, are respectively located ~100 m, ~50 m and ~20 m below a relatively undisturbed seafloor (Fig. 4b). The three glide planes are separated by steep scarps and seem to be planar, with only a few undulations observed in the study area (Figs. 3a and b). On the Parasound profiles, a thin layer (~10-15 m) of slide deposits characterised by chaotic reflections is separated by glide planes from the underlying strata (Figs. 4a, b, 5b and c).

4.1.3 Plateaus

Two large plateaus are identified in the central part of the study area; Plateau I and Plateau II (Figs. 2, 3a and b). Plateau I is located in the northeastern part of the study area. It has an average length of 7 km and an average width of 4 km. Plateau II is located in the southeastern part of the study area, showing an average length of 14 km and an average width of 6 km. The height of Plateaus I and II is approximately 30 m above the level of GP I. The morphology of both plateaus reveals the presence of several slide blocks (Figs. 3a and b).

4.1.4 Slide lobes

Slide lobes as defined based on data from the Storegga Slide (Haflidason et al., 2004) are individual or group of mass movements. Two slide lobes are visible in the upper headwall on the sidescan sonar mosaic (Fig. 6).

One lobe is located to the south of the headwall, whereas a second lobe is located on the northwestern part of Plateau I.

4.1.5 Hummocky topography with slide blocks

Slide blocks are widespread in the upper headwall and particularly found above GP I and GP II (Fig. 3). The deposits show a characteristic hummocky geometry especially in lower half of GP I (Fig. 3c). In contrast, the shallowest part of the GP I area is relatively smooth (Figs. 3a and b). The slide blocks can also be identified from Parasound profiles crossing the deeper part of GP I (Fig. 5c). The diameter of the imaged blocks reaches a maximum of 500 m and a maximum height of 35 m (Fig. 3c).

4.2 Acoustic facies

Sidescan sonar data provide a detailed image of seafloor morphology and texture in the upper headwall of the Sahara Slide Complex (Figs. 6 and 7). Based on observed variations in backscatter character, we defined four different types of acoustic facies.

4.2.1 Facies 1: Smooth, medium backscattering seafloor

Facies 1 is characterised by homogenous, medium backscatter values (Figs. 6 and 8a). Facies 1 is located in regions of undisturbed slope strata, upslope of imaged headwall scarps (Fig. 7), where stratified slope sediments are imaged on sub-bottom profiler data (Figs. 6 and 8b). We interpret these areas as comprising undisturbed fine-grained hemipelagites.

4.2.2 Facies 2: Medium to high backscattering seafloor with slight variations in backscatter

Facies 2 is characterised by a smooth, medium to high backscatter seafloor, with small variations in backscatter strength. It mainly occurs on GP I and II (Figs. 6 and 7). Facies 2 is interpreted to be associated with the presence of smooth glide planes over which sediments were evacuated. Minor variations in backscatter strength indicate the presence of thin slide deposits. Sub-bottom profile data crossing Facies 2 also shows the seafloor as a relatively smooth, regular surface (Fig. 4a).

4.2.3 Facies 3: Sediment ridges and crown cracks

Facies 3 shows alternating high and low backscatter values, which highlight the presence of elongated topographical highs that are oriented parallel to the headwall (Figs. 8a and 9a). These elongated features are irregular and of variable sizes, and their length varies from a few tens of meters to several kilometers. Most of these elongated features are observed above GP II and GP III in the southeastern and northeastern parts of the upper headwall, respectively (Figs. 6 and 7).

Facies 3 comprises sediment ridges based on their distribution and morphology. Their orientation is parallel to the headwall. The dimension of sediment ridges to the northeast is relatively small when compared to the region to the southeast of the upper headwall (Figs. 8a and 9a). Sediment ridges can be more than 1 km in length to the southeast of the upper headwall (Fig. 9a). Thus, Facies 3 can be further divided into two sub-facies 3a and 3b, based on the dimensions of sediment ridges. Facies 3a represents the area with small-scale (<500 m in length) sediment ridges and Facies 3b indicates the area with large-scale (>1 km in length) sediment ridges. The sediment ridges show a closer spacing in the areas nearest to the headwall, while their sizes and spacing increases downslope (Fig. 9a).

Crown cracks are visible in undisturbed strata behind the upper headwall (Figs. 8a and 9b). A secondary crown crack is identified ~430 m away from the headwall to the southeast (Fig. 9a). It has a length of 545 m and a width of 51 m (Fig. 9b).

4.2.4 Facies 4: Slide blocks and basal striae

Facies 4 is observed over GP I and GP II (Figs. 6 and 7). Slide blocks are imaged as high backscatter areas with shadow zones and are widespread over GP I and GP II (Figs. 6 and 10a). The size of the slide blocks varies greatly, ranging from 500-m long features to smaller blocks <40 m in length. Blocks of Facies 4 are identified in sub-bottom profiler data as a hummocky seafloor (Fig. 10b). Facies 4 can be further subdivided into Facies 4a, areas dominated by small slide blocks <40 m, and Facies 4b, areas dominated by large slide blocks >40 m.

Facies 4 also includes striations, which are elongate areas (stripes) of smooth backscatter. Slide blocks are usually found at the end of these striations (Fig. 6). Usually the striations show slightly higher backscatter values compared to background strata (Figs. 6 and 10a). The striations are interpreted as load casts formed by moving slide blocks because major blocks are found at their downslope terminations. The moving blocks eroded the glide plane through large distances to form the elongate basal striations. The NW-SE orientation of these basal striations suggests a predominant direction of mass movement to the northwest, away from the headwall (Fig. 10a), which is consistent with the direction of the maximum slope gradient.

4.3 Volume estimation of the mass movements

Estimates of the affected area and volume of strata involved in mass movements are critical for the assessment of their tsunamigenic potential (Watts et al., 2005). The hazard potential usually increases with the volume of the mass movements as the magnitude of tsunamis that were generated by landslides is mainly controlled by the size, initial acceleration, maximum velocity and pathway of the displaced mass movements (Harbitz et al., 2006).

As the interpreted bathymetry data do not provide full coverage of the upper headwall, we can only provide an estimate of 1700 km^2 for the area of the landslide scar enclosed by the upper headwall area (Fig. 2a). GP I has an area of 1485 km^2. GP II covers a total area of 130 km^2, including Plateau I with 25 km^2, Plateau II with 75 km^2

and the area affected by large-scale sediment ridges with 30 km^2. GP III has an area of 85 km^2 in the northeastern part affected by small-scale sediment ridges. The total volume of remobilized strata in the upper headwall is ~150 km^3. The volumes of removed sediment on GP I, II and III are approximately 140 km^3, 7 km^3 and 3 km^3, respectively. The calculated volume of missing sediments over GP I and II is reasonably accurate because bathymetric data fully cover this area, although we cannot be sure on the pre-failure morphology. The volume of missing sediments above GP I is a minimum estimate because the bathymetry indicates that the evacuation zone continues further downslope, beyond the limit of our data coverage.

4.4 Timing of the mass movements

In total, ten gravity cores were taken in the headwall area. Nine of the ten cores were taken in the landslide area (Fig. 2a). They all contain debrite deposits dominated by clasts (Fig. 11). Gravity core P395-07-1 shows a distinct thin (~4 cm) sedimentary drape on top of the underlying debris (Fig. 11). The core did not reach the glide plane. The sedimentary drape contains well-oxidised sediment (beige-pink foraminifera-bearing mud). No drape being thick enough for dating (>2cm) was identified in any other core targeting the landslide deposits. As described in the method section, we assume the loss of no more than 10 cm of surface sediments occurred at any point in our coring.

A sample for dating the undisturbed drape on top of the landslide deposits were taken at 3 cm bsf in Core P395-07-1, which is about 1 cm above the slide deposits (Fig. 11). The measured age for this sample is 1840 ± 23 years BP (Table 1). This age is not representing the failure age but a minimum age. A common procedure for calculating the failure age is to add the time needed for the deposition of the undisturbed deposits between the top of the landslide deposits and the sample location used for dating. Sedimentation rate is needed for this approach. The sample in Core P395-07-1 is taken only about 1 cm above the slide deposits. If we assume that the top of the core represents the seafloor and the sample is 3 cm bsf, we calculate a sedimentation rate of only ~1.63 cm/ka assuming a constant sedimentation rate. A value of ~1.63 cm/ka for the sedimentation rate is significantly lower than documented in previous studies from nearby areas (~5 cm/ka on average after, Bertrand et al., 1996; Weaver et al. 2000; Georgiopoulou et al., 2009). The most likely explanation for this discrepancy is that surface sediments were lost during gravity coring (as stated above). Using sedimentation rates of 1.63 cm/ka and 5 cm/ka, age corrections would be 0.6 ka and 0.2 ka, respectively, following the approach described in the method section. As a result, the corrected age of the slide deposits at the location of Core P395-07-1 is ~2.24±0.2 ka. We are aware that a single date may not represent the age of the entire failure. However, we point out that cores beneath the headwall are available at various locations (Fig. 2a), and none of these additional cores shows an undisturbed drape thick enough to allow a reliable dating of the Sahara Slide Complex. Even considering a loss of about 10 cm of surface sediments, an age of ~ 2 ka for the failure would still be estimated by assuming a sedimentation rate of 5 cm/ka. The missing drape may indicate an even younger age.

In order to support a young age of the failure, we dated one clast being part of the debrite deposits in core P395-04-1. The age of this clast is 6172 ± 78 years BP (Fig. 11, Tab. 1). This clast provides a maximum age for the slide event on GP I because it comprises disrupted slope material deposited prior to the failure. Hence, this date also suggests a young age of the failure.

In summary, we consider the entire failure of the upper headwall area of the Sahara Slide to have occurred in Late Holocene times. This age contrasts to the estimate of ~50-60 ka revealed in previous studies for the distal Sahara Slide deposits (Gee et al, 1999; Georgiopoulou et al., 2010).

5. Discussion

5.1 Types of mass movements at the headwall of the Sahara Slide Complex

Differences in morphology in the GP I, II and III areas indicate distinct mass-movement types (e.g. Micallef et al., 2007; Baeten et al., 2013) (Figs. 3 and 6). The elongate ridges and troughs indicate widespread extension, leading to gravitational spreading. Gravitational spreading has a characteristic morphology, with repetitive ridges and troughs oriented parallel to scarps and perpendicular to the direction of mass movement (Micallef et al., 2007; Baeten et al., 2013). Gravitational spreading is a common and pervasive type of mass movement, which has been identified (among other areas) in the Ormen Lange area of the Storegga Slide (Kvalstad et al., 2005; Micallef et al., 2007), the Hinlopen Slide area (Vanneste et al., 2006), the St. Pierre Slope (Piper et al., 1999), the continental slope offshore Mauritania (Krastel et al., 2007), and at an outcrop in SE Crete (Alves and Lourenço, 2010; Alves, 2015). At the upper headwall of the Sahara Slide Complex, the morphology of flat-topped glide planes, with no or very little debris remaining on them, and internal architecture showing glide planes parallel to the stratigraphy, reveal that translational sliding also took place which commonly occurs along a planar failure surface, with little rotation or backward tilting (Varnes, 1978). Translational slides often disintegrate into debris flows (Piper et al., 1999). This is also observed for the Sahara Slide Complex, where elongated ridges are disintegrated downslope into blocks of decreasing size, leading to full transformation into debris flow and turbidity currents (Georgiopoulou et al., 2009). Many submarine landslides identified on continental margins are translational in nature and are developed retrogressively in multiple episodes of slope failure, e.g. the Hinlopen Slide on the Arctic Ocean margin (Vanneste et al., 2006), the Mauritania Slide Complex on the Northwest African continental margin (Krastel et al., 2007) and Storegga Slide on the Norwegian continental margin (Haflidason et al., 2004). We believe similar processes took place in the Sahara Slide Complex.

Gravitational spreading occurred mainly in the northeastern (along GP III) and southeastern (along GP II) parts of the upper headwall, where multiple sediment

ridges are observed. The size of sediment ridges vary between GP II and III, with ridges being smaller on GP III compared to GP II (Figs. 8a and 9a). Due to the lack of deeper sediment samples, we cannot address the specific reasons for these differences. The scale of the sediment ridges has been proposed to be controlled by several factors including gravitationally induced stress, angle of internal friction of the sediment, pore pressure escape, and basal friction (Micallef et al., 2007).

Translational sliding occurred in the central part of the slide scar on GP I, and on two large plateaus along GP II (Figs. 6 and 7). GP I and II are located at two different stratigraphic levels, but present similar morphologies. Both areas are characterised by widespread large sediment blocks and elongated striations in some places (Facies 4b, Fig. 10a), whereas other places show small blocks and thin debris deposits (Facies 4a, Fig. 10a). This observation provides robust evidence that mass movement processes on GP I and II are similar. Sediment blocks likely resulted from the disintegration of failed strata but they do not disintegrate fully as they are clearly seen as blocks in the morphological data. The striations imply bottom contact causing erosion and drag forces, suggesting that the blocks moved not very fast. This is further supported by the fact that the blocks are found relatively close to the headwall. However, full disintegration seems to occur in places (Facies 4a) suggesting a higher energy regime for these areas. Hence, the translational sliding on GP I and II may represent "fast sliding" of failed slope deposits at least in the areas where full disintegration is taking place, while relative "slow sliding" (i.e. spreading) took place above GP III and small parts of GP II, forming detached sediment ridges. The cracks identified away the headwall to the southeast suggest the presence of sediment slabs, highlighting the preferential region for future translational sliding (Laberg et al., 2013). The presence of cracks may also indicate a permanent state of instability on the continental slope.

5.2 Evidence for multiple slope failures

The upper headwall of the Sahara Slide shows a complex morphology in bathymetric and sidescan sonar data (Figs. 2a and 6). The exposed headwall scarps and the lack of slide debris close to the headwall scarps indicate that the upper headwall has been evacuated (Fig. 2a). This complex morphology is evidence for the formation of the upper headwall during multi-stage failure events. These events are results of two different types of mass movements that occurred in the upper headwall; translational sliding and gravitational spreading. We interpret gravitational spreading in the GP I area as a direct consequence of translational sliding further downslope due to the lack of support from removed sediments. In addition, we consider that that retrogressive failure formed the upper headwall of the Sahara Slide Complex. Retrogressive failures have been identified for many landslides including the Humboldt Slide on the northern California continental margin (Gardner et al., 1999) and the Storegga Slide on the Norwegian continental margin (Kvalstad et al., 2005).

The relationship between the upper and lower headwalls, however, remains unclear as no age data and detailed acoustic data are available for the latter region. The distal deposits of the Sahara Slide are dated at 50-60 ka (Gee et al., 1999; Georgiopoulou et al., 2010), a date much older than the age estimated for the upper headwall in this study. A plausible explanation for this discrepancy in ages is that the lower headwall may have been formed in association with the 50-60 ka failure event, whereas the upper headwall is the result of a much younger instability. Sparse sediment echo-sounder data suggest younger failures of the upper headwall compared to the lower headwall. In this case, we would consider slope failure of the upper and lower headwalls as independent events due to the long time spanning these two events. The observed distance of ~50 km between the two headwalls would also be unusually large for a retrogressive failure (e.g. Imbo et al., 2003; Locat et al., 2009; Baeten et al., 2013).

An alternative explanation is that both headwalls were formed 50-60 ka ago, and the younger failure of the upper headwall represents a phase of reactivation of this latter area. This would imply that failure of both headwalls is somewhat related, but more data is necessary to investigate this hypothesis.

5.3 Possible preconditioning factors and triggers for slope instability at the upper headwall of the Sahara Slide Complex

Various preconditioning factors have been proposed as promoting failures on continental margins, including high sedimentation rates (Leynaud et al., 2007) and the presence of weak layers (Baeten et al., 2014). Recent modeling results from Urlaub et al. (2015) suggest that sedimentation rates in the Sahara Slide area (~5 cm/ka) are insufficient to destabilise the slope. Weak layers were defined by Locat et al. (2014) as sediment layers that have lower strength compared to adjacent units, and can provide a potential focus for the development of a surface of rupture. The presence of weak layers have been considered as an important preconditioning factor for the generation of submarine landslides in several regions such as the slopes at Finneidfjord, northern Norway (L'Heureux et al., 2012) and the Mauritania Slide area (Antobreh and Krastel, 2007). Slope failure in the upper headwall of the Sahara Slide Complex occurred along three pronounced and widespread glide planes; we consider this observation as evidence for the presence of weak layers at distinct depths below the seafloor. However, we do not know the composition of these layers due to missing sediment samples.

One possibility could be the presence of sediment layers with particularly high compressibilities as it has been proposed to play a vital role for the instabilities offshore Northwest Africa (Urlaub et al., 2015). Organic-rich sediments typically have high compressibilities (Booth and Dahl, 1986; Bennett et al., 1985). In fact, the study area is affected by a strong upwelling system driven by the Northeast Trade Winds (Cropper et al., 2014), which results in high primary productivity and the deposition of organic-rich sediments. This upwelling system typically reached its maximum productivity during deglaciations (Bertrand et al., 1996), which may explain

the different stratigraphic depths of the glide planes.

Our new data do not provide any information on the final trigger of the slope failure. However, we consider seismicity possibly related to the reactivation of old fracture zone or the evolution of the Canary Islands as most likely trigger. The Canary Islands and surrounded areas are presently seismically active, characterised by small and medium-size earthquakes (Ibáñez et al., 2012). The study area is ~300 km away from the Canary Islands and earthquakes associated with these same islands might be a triggering mechanism for the slide events in the upper headwall of Sahara Slide. Thus, we conclude that the presence of weak layers consisting of a particular sediment type is the main potential preconditioning factor, but the final triggering of the failures remains speculative.

5.4 Timing of the failure and implications for geohazard assessment

Several authors have discussed potential relationships between sea-level and landslide frequency (Owen et al., 2007; Lee, 2009; Leynaud et al., 2009; Urlaub et al., 2013). Based on a compilation of available ages for landslides on the Atlantic Ocean margin, Lee (2009) stated that the continental margin is relatively stable at present, partly related to the stable sea level. Only 2-3 landslides are documented during the past 5000 years; the frequency of landslide occurrence for this period is less by a factor of 1.7 to 3.5 compared to the time of sea-level rise after the last glaciation. Major landslides off Northwest Africa were also related to periods of low or rising sea level (Krastel et al., 2012). The distal deposits of the Sahara Slide are dated at 50-60 ka before present, which was during a period of rising sea level (Gee et al., 1999; Georgiopoulou et al., 2007).

A link between sea-level and landslide frequency, however, is negated by Urlaub et al. (2013) based on a statistical analysis of a global compilation of available ages for large (>1 km^3) continental margin landslides. Urlaub et al. (2013) stated that the global data set did not show statistically significant patterns, trends or clusters in landslide abundance but they note that significantly fewer events occurred in the past 6 ka. Urlaub et al. (2013) also analysed landslides at the Northwest African continental margin as subset of the global data set concluding that ages are nearly evenly distributed without any clustering or increased frequency. Our study suggests that the failure of the upper headwall of the Sahara Slide is only ~2.24±0.2 ka old. Despite the fact, that this age is only based on one dated sample, we consider the missing undisturbed drape on top of the landslide deposits at all other cores as very strong evidence for a similarly young age for the entire failure of the upper headwall area during a period of constantly high sea level. This interpretation is further supported by the occurrence of debrite deposits of a similar age up to 250 km downslope of the headwall and an associated turbidite extending for more than 700 km (Georgiopoulou et al., 2009). Georgiopoulou et al. (2009) suggest that the linked turbidite-debrite bed was formed during the recent failure of the Sahara Slide headwall.

While we consider the upper and lower headwall area of the Sahara Slide complex as independent events, the failure of the upper headwall of the Sahara Slide Complex most likely occurred in several retrogressive stages as indicated by glide planes at different levels and multiple headwalls. A retrogressive failure has large implications for the tsunamigenic potential. Tsunamigenic potential in the Sahara Slide would be larger if the slide events occurred simultaneously, compared to the case of retrogressive landslides (Harbitz et al., 2014). A key observation in the study area is that missing volumes on top of individual glide planes are large (> 100 km^3). Relatively small failures in the past have triggered significant tsunamis. In the case of the 1998 event at Papua New Guinea, Tappin et al. (2001) concluded the tsunami, which resulted in the deaths of over 2000 people, was a direct result of a slump with an estimated volume of 5-10 km^3. The 11,500-year BP BIG'95 landslide detected in the Mediterranean Sea involved a total volume of 26 km^3 (Lastras et al., 2004; Urgeles et al., 2006). Even such failures with small volume landslide deposits may cause catastrophic tsunamis based on the recent tsunami simulations (Løvholt et al., 2014). Modelling of the 165 km^3 Currituck landslide (Locat et al., 2009), also revealed potential for a devastating tsunami (Geist et al., 2009). The volumes of the removed sediments on GP I, II and III in the upper headwall of Sahara Slide are approximately 140 km^3, 7 km^3 and 3 km^3, respectively. It is unlikely, that the failure on top of GP III occurred as a single event, but the examples above show that individual failures of the Sahara Slide complex were large enough to present a significant tsunamigenic potential, even if occurring in relatively large water depths (~2000 m) (Lo Iacono et al., 2012; Harbitz et al., 2014). In addition, Georgiopoulou et al. (2009) observed turbidite deposits up to 700 km downslope of the Sahara Slide headwall. They interpret this turbidite to have formed by recent failure of the Sahara Slide headwall; either by the near-simultaneous generation of a debris flow and turbidity current, or by entrainment of water into the debris flow leading to the generation of a turbidity current. These processes and the long run-out distance of the turbidity current suggest a relatively fast moving landslide body, High flow velocities have high tsunamigenic potential (Harbitz et al., 2006). Such an observation, in combination with the young age of the failure, calls for a reassessment of landslide hazards along the Northwest African continental margin, estimated to be low in previous studies (Lee, 2009). However, such a reassessment is beyond the scope of this manuscript.

6. Conclusions

A combination of high-resolution bathymetry, sidescan sonar, sub-bottom profiler data, and sediment cores allowed to reconstruct the failure behavior of the upper headwall of Sahara Slide Complex on the continental margin offshore Northwest Africa. The main conclusions of this study are:

(1) The upper headwall was evacuated, and several morphological elements (e.g., slide scarps, glide planes, plateaus, lobes and slide blocks) are identified on the modern seafloor. The volume of the evacuated area exceeds 150 km^3.

(2) The morphology and configuration of the upper headwall is the result of multiple failure events probably occurring mainly as spreading and translational sliding on three different glide planes retrogressively. The presence of weak layers is considered as the main preconditioning factor for instability in the Sahara Slide Complex.

(3) The slide processes on glide plane I and II record the generation of disintegrated slide blocks of different scales, indicating relatively "fast sliding". In contrast, the slide processes on glide plane III were mainly characterised by spreading resulting in widespread sediment ridges, troughs and cracks upslope (in the unfailed strata) as relative "slow sliding".

(4) The upper headwall of the Sahara Slide Complex was active (or reactivated) in the late Holocene about 2 ka BP during times of a stable sea-level high stand. The failure may be the largest of Holocene failures worldwide. The young age is an important contribution to the ongoing debate on potential relationships between sea-level and landslide frequency, as it shows that very large landslide do occur during times of a stable sea level high stand. The young age in combination with the large volume calls for a reassessment of the slope instability and the tsunamigenic potential along the margin offshore Northwest Africa and other continental margins that are considered currently stable.

(5) Crown cracks indicate the slope may not be at equilibrium and instability may still be ongoing.

Acknowledgments

We thank the crews and captains of RV Poseidon Cruise P395 and RV Maria S. Merian Cruise MSM11/4. Financial support was provided by the Deutsche Forschungsgemeinschaft (DFG). W. Li is funded by the China Scholarship Council (CSC). We also acknowledge Michele Rebesco (Editor), Marc De Batist (reviewer) and one anonymous reviewer for their constructive comments that clarified the manuscript.

Reference

Alves, T.M., 2015. Submarine slide blocks and associated soft-sediment deformation in deep-water basins: A review. Marine and Petroleum Geology 67, 262-285.

Alves, T.M., Lourenço, S.D.N., 2010. Geomorphologic features related to gravitational collapse: Submarine landsliding to lateral spreading on a Late Miocene–Quaternary slope (SE Crete, eastern Mediterranean). Geomorphology 123, 13-33.

Antobreh, A.A., Krastel, S., 2007. Mauritania Slide Complex: morphology, seismic characterisation and processes of formation. International Journal of Earth Sciences 96, 451-472.

Baeten, N.J., Laberg, J.S., Forwick, M., Vorren, T.O., Vanneste, M., Forsberg, C.F., Kvalstad, T.J., Ivanov, M., 2013. Morphology and origin of smaller-scale mass movements on the continental slope off northern Norway. Geomorphology 187, 122-134.

Baeten, N.J., Laberg, J.S., Vanneste, M., Forsberg, C.F., Kvalstad, T.J., Forwick, M., Vorren, T.O., Haflidason, H., 2014. Origin of shallow submarine mass movements and their glide planes—Sedimentological and geotechnical analyses from the continental slope off northern Norway. Journal of Geophysical Research: Earth Surface 119, 2335-2360.

Bennett, R.H., Lehman, L., Hulbert, M.H., Harvey, G.R., Bush, S.A., Forde, E.B., Crews, P., Sawyer, W.B., 1985. Interrelationships of organic carbon and submarine sediment geotechnical properties. Marine Geotechnology 6, 61-98.

Berndt, C., Costa, S., Canals, M., Camerlenghi, A., de Mol, B., Saunders, M., 2012. Repeated slope failure linked to fluid migration: The Ana submarine landslide complex, Eivissa Channel, Western Mediterranean Sea. Earth and Planetary Science Letters 319-320, 65-74.

Bertrand, P., Shimmield, G., Martinez, P., Grousset, F., Jorissen, F., Paterne, M., Pujol, C., Bouloubassi, I., Buat Menard, P., Peypouquet, J.P., Beaufort, L., Sicre, M.A., Lallier-Verges, E., Foster, J.M., Ternois, Y., Program O.P.o.t.S., 1996. The glacial ocean productivity hypothesis: the importance of regional temporal and spatial studies. Marine Geology 130, 1-9.

Bickert, T., cruise participants, 2011. Pre-Site Survey for an IODP cruise Neogene Paleoclimate and sediment transport at the continental margin of NW Africa - Cruise No. MSM11/2 - March 14 - April 09, 2009 - Dakar (Senegal) - Las Palmas (Canary Islands, Spain). MARIA S. MERIAN Berichte, MSM11/2, 53 pp., DFG-Senatskommission für Ozeanographie, DOI: 10.2312/cr_msm11_2.

Booth, J.S., Dahl, A.G., 1986. A note on the relationships between organic matter and some geotechnical properties of a marine sediment. Marine Geotechnology 6, 281-297.

Cropper, T.E., Hanna, E., Bigg, G.R., 2014. Spatial and temporal seasonal trends in coastal upwelling off Northwest Africa, 1981–2012. Deep Sea Research Part I: Oceanographic Research Papers 86, 94-111.

Embley, R.W., 1982. Anatomy of Some Atlantic Margin Sediment Slides and Some Comments on Ages and Mechanisms, in: Saxov, S., Nieuwenhuis, J.K. (Eds.), Marine Slides and Other Mass Movements. Springer US, Boston, MA, pp. 189-213.

Förster, A., Ellis, R.G., Henrich, R., Krastel, S., Kopf, A.J., 2010. Geotechnical characterization and strain analyses of sediment in the Mauritania Slide Complex, NW-Africa. Marine and Petroleum Geology 27, 1175-1189.

Gardner, J.V., Prior, D.B., Field, M.E., 1999. Humboldt Slide — a large shear-dominated retrogressive slope failure. Marine Geology. 154, 323–338.

Gee, M.J.R., Masson, D.G., Watts, A.B., Allen, P.A., 1999. The Saharan debris flow: an insight into the mechanics of long runout submarine debris flows. Sedimentology 46, 317-335.

Gee, M.J.R., Masson, D.G., Watts, A.B., Mitchell, N.C., 2001. Passage of debris flows and turbidity currents through a topographic constriction: seafloor erosion and deflection of flow pathways. Sedimentology 48, 1389-1409.Geist, E.L., Lynett, P.J., Chaytor, J.D., 2009. Hydrodynamic modeling of tsunamis from the Currituck landslide. Marine Geology 264, 41-52.

Georgiopoulou, A., Krastel, S., Masson, D.G., Wynn, R.B., 2007. Repeated Instability Of The NW African Margin Related To Buried Landslide Scarps, in: Lykousis, V., Sakellariou, D., Locat, J. (Eds.), Submarine Mass Movements and Their Consequences: 3 International Symposium. Springer Netherlands, Dordrecht, pp. 29-36.

Georgiopoulou, A., Masson, D.G., Wynn, R.B., Krastel, S., 2010. Sahara Slide: age, initiation and processes of a giant submarine slide. Geochemistry, Geophysics, Geosystems 11, 1-22.

Georgiopoulou, A., Wynn, R.B., Masson, D.G., Frenz, M., 2009. Linked turbidite–debrite resulting from recent Sahara Slide headwall reactivation. Marine and Petroleum Geology 26, 2021-2031.

Golbeck, I., 2010. The Sahara Slide Complex. Unpublished thesis. Department of Geosciences, University of Bremen, 137 pp.

Haflidason, H., Sejrup, H.P., Nygård, A., Mienert, J., Bryn, P., Lien, R., Forsberg, C.F., Berg, K., Masson, D., 2004. The Storegga Slide: architecture, geometry and slide development. Marine Geology 213, 201-234.

Harbitz, C.B., Løvholt, F., Bungum, H., 2014. Submarine landslide tsunamis: how extreme and how likely? Natural Hazards 72, 1341-1374.

Harbitz, C.B., Løvholt, F., Pedersen, G., Masson, D.G., 2006. Mechanisms of tsunami generation by submarine landslides: a short review. Norw. J. Geol. 86, 255-264

Hayes, D.E., Rabinowitz, P.D., 1975. Mesozoic magnetic lineations and the magnetic quiet zone off northwest Africa. Earth and Planetary Science Letters 28, 105-115.

Henrich, R., Hanebuth, T.J.J., Krastel, S., Neubert, N., Wynn, R.B., 2008. Architecture and sediment dynamics of the Mauritania Slide Complex. Marine and Petroleum Geology 25, 17-33.

Holz, C., Stuut, J.b.W., Henrich, R., 2004. Terrigenous sedimentation processes along the continental margin off NW Africa: implications from grain-size analysis of seabed sediments. Sedimentology 51, 1145-1154.

Ibáñez, J.M., De Angelis, S., Díaz-Moreno, A., Hernández, P., Alguacil, G., Posadas, A., Pérez, N., 2012. Insights into the 2011–2012 submarine eruption off the coast of El Hierro (Canary Islands, Spain) from statistical analyses of earthquake activity. Geophysical Journal International 191, 659-670.

Imbo, Y., De Batist, M., Canals, M., Prieto, M.J., Baraza, J., 2003. The Gebra Slide: a submarine slide on the Trinity Peninsula Margin, Antarctica. Marine Geology 193, 235-252.

Krastel, S., Behmann, J.-H., Völker, D., Stipp, M., Berndt, C., Urgeles, R., Chaytor, J., Huhn, K., Strasser, M., Harbitz, C.B., 2014. Submarine mass movements and their consequences. 6th International Symposium. Advances in Natural and Technological Research 37, pp 683.

Krastel, S., cruise participants, 2011. FS POSEIDON Fahrtbericht/Cruise Report P395-Sahara Slide Complex, 04.02.-19.02.2010 Las Palmas - Las Palmas (Spain). IFM-GEOMAR Report, 50. IFM-GEOMAR, Kiel, 43 pp. DOI 10.3289/IFM-GEOMAR_REP_50_2011.

Krastel, S., Wynn, R.B., Georgiopoulou, A., Geersen, J., Henrich, R., Meyer, M., Schwenk, T., 2012. Large-Scale Mass Wasting on the Northwest African Continental Margin: Some General Implications for Mass Wasting on Passive Continental Margins. 189-199.

Krastel, S., Wynn, R.B., Hanebuth, T.J.J., Henrich, R., Holz, C., Meggers, H., Kuhlmann, H., Georgiopoulou, A., Schulz, H.D., 2006. Mapping of seabed morphology and shallow sediment structure of the Mauritania continental margin, Northwest Africa: some implications for geohazard potential. Norwegian Journal of Geology 86, 163-176.

Kvalstad, T.J., Andresen, L., Forsberg, C.F., Berg, K., Bryn, P., Wangen, M., 2005. The Storegga slide: evaluation of triggering sources and slide mechanics. Marine and Petroleum Geology 22, 245-256.

L'Heureux, J.-S., Longva, O., Steiner, A., Hansen, L., Vardy, M.E., Vanneste, M., Haflidason, H., Brendryen, J., Kvalstad, T.J., Forsberg, C.F., Chand, S., Kopf, A., 2012. Identification of Weak Layers and Their Role for the Stability of Slopes at Finneidfjord, Northern Norway, in: Yamada, Y., Kawamura, K., Ikehara, K., Ogawa, Y., Urgeles, R., Mosher, D., Chaytor, J., Strasser, M. (Eds.), Submarine Mass Movements and Their Consequences: 5th International Symposium. Springer Netherlands, Dordrecht, pp. 321-330.

Løvholt, F., Harbitz, C.B., Vanneste, M., Blasio, F.V., Urgeles, R., Iglesias, O., Canals, M., Lastras, G., Pedersen, G., Glimsdal, S., 2014. Modeling Potential Tsunami Generation by the BIG'95 Landslide, in: Krastel, S., Behrmann, J.-H., Völker, D., Stipp, M., Berndt, C., Urgeles, R., Chaytor, J., Huhn, K., Strasser, M.,

Harbitz, B.C. (Eds.), Submarine Mass Movements and Their Consequences: 6th International Symposium. Springer International Publishing, Cham, pp. 507-515.

Laberg, J.S., Baeten, N.J., Lågstad, P., Forwick, M., Vorren, T.O., 2013. Formation of a large submarine crack during the final stage of retrogressive mass wasting on the continental slope offshore northern Norway. Marine Geology 346, 73-78.

Lamarche, G., Mountjoy, J., Bull, S., Hubble, T., Krastel, S., Lane, E., Micallef, A., Moscardelli, L., Mueller, C., Pecher, I., Woelz, S., 2016. Submarine mass movements and their consequences. 7th International Symposium. Advances in Natural and Technological Research, 41, pp 621.

Lange, C.B., Romero, O.E., Wefer, G., Gabric, A.J., 1998. Offshore influence of coastal upwelling off Mauritania, NW Africa, as recorded by diatoms in sediment traps at 2195 m water depth. Deep Sea Research Part I: Oceanographic Research Papers 45, 985-1013.

Lastras, G., Canals, M., Urgeles, R., De Batist, M., Calafat, A.M., Casamor, J.L., 2004. Characterisation of the recent BIG'95 debris flow deposit on the Ebro margin, Western Mediterranean Sea, after a variety of seismic reflection data. Marine Geology 213, 235-255.

Lee, H.J., 2009. Timing and occurrence of large submarine landslides on the Atlantic Ocean Margin. Marine Geology 264, 53-64.

Leynaud, D., Mienert, J., Vanneste, M., 2009. Submarine mass movements on glaciated and non-glaciated European continental margins: A review of triggering mechanisms and preconditions to failure. Marine and Petroleum Geology 26, 618-632.

Leynaud, D., Sultan, N., Mienert, J., 2007. The role of sedimentation rate and permeability in the slope stability of the formerly glaciated Norwegian continental margin: the Storegga slide model. Landslides 4, 297-309.

Li, W., Wu, S., Völker, D., Zhao, F., Mi, L., Kopf, A., 2014. Morphology, seismic characterization and sediment dynamics of the Baiyun Slide Complex on the northern South China Sea margin. Journal of the Geological Society 171, 865-877.

Lo Iacono, C., Gràcia, E., Zaniboni, F., Pagnoni, G., Tinti, S., Bartolomé, R., Masson, D.G., Wynn, R.B., Lourenço, N., Pinto de Abreu, M., Dañobeitia, J.J., Zitellini, N., 2012. Large, deepwater slope failures: Implications for landslide-generated tsunamis. Geology 40, 931-934.

Locat, J., Lee, H., ten Brink, U.S., Twichell, D., Geist, E., Sansoucy, M., 2009. Geomorphology, stability and mobility of the Currituck slide. Marine Geology 264, 28-40.

Locat, J., Leroueil, S., Locat, A., Lee, H., 2014. Weak Layers: Their Definition and Classification from a Geotechnical Perspective, in: Krastel, S., Behrmann, J.-H., Völker, D., Stipp, M., Berndt, C., Urgeles, R., Chaytor, J., Huhn, K., Strasser, M., Harbitz, C.B. (Eds.), Submarine Mass Movements and Their Consequences. Springer International Publishing, pp. 3-12.

Mangerud, J., Gulliksen, S., 1975. Apparent radiocarbon ages of recent marine shells from Norway, Spitsbergen, and Arctic Canada. Quaternary Research 5, 263-273.Maslin, M., Owen, M., Day, S., Long, D., 2004. Linking continental-slope failures and climate change: testing the clathrate gun hypothesis. Geology 32, 53-56.

Masson, D.G., Harbitz, C.B., Wynn, R.B., Pedersen, G., Løvholt, F., 2006. Submarine landslides: processes, triggers and hazard prediction. Philosophical Transactions of the Royal Society of London A: Mathematical, Physical and Engineering Sciences 364, 2009-2039.

Meyer, M., Geersen, J., Krastel, S., Schwenk, T., Winkelmann, D., 2012. Dakar Slide Offshore Senegal, NW-Africa: Interaction of Stacked Giant Mass Wasting Events and Canyon Evolution, in: Yamada, Y., Kawamura, K., Ikehara, K., Ogawa, Y., Urgeles, R., Mosher, D., Chaytor, J., Strasser, M. (Eds.), Submarine Mass Movements and Their Consequences. Springer Netherlands, pp. 177-188.

Micallef, A., Masson, D.G., Berndt, C., Stow, D.A.V., 2007. Morphology and mechanics of submarine spreading: A case study from the Storegga Slide. Journal of Geophysical Research: Earth Surface 112, 1-21.

Moernaut, J., De Batist, M., 2011. Frontal emplacement and mobility of sublacustrine landslides: Results from morphometric and seismostratigraphic analysis. Marine Geology 285, 29-45.

Owen, M., Day, S., Maslin, M., 2007. Late Pleistocene submarine mass movements: occurrence and causes. Quaternary Science Reviews 26, 958-978.

Pereira, R., Alves, T.M., 2011. Margin segmentation prior to continental break-up: A seismic–stratigraphic record of multiphased rifting in the North Atlantic (Southwest Iberia). Tectonophysics 505, 17-34.

Piper, D.J.W., Aksu, A.E., 1987. The source and origin of the 1929 grand banks turbidity current inferred from sediment budgets. Geo-Marine Letters 7, 177-182.

Piper, D.J.W., Cochonat, P., Morrison, M.L., 1999. The sequence of events around the epicentre of the 1929 Grand Banks earthquake: initiation of debris flows and turbidity current inferred from sidescan sonar. Sedimentology 46, 79-97.

Reimer, P.J., Bard, E., Bayliss, A., Beck, J.W., Blackwell, P.G., Bronk Ramsey, C., Grootes, P.M., Guilderson, T.P., Haflidason, H., Hajdas, I., Hatté, C., Heaton, T.J., Hoffmann, D.L., Hogg, A.G., Hughen, K.A., Kaiser, K.F., Kromer, B., Manning, S.W., Niu, M., Reimer, R.W., Richards, D.A., Scott, E.M., Southon, J.R., Staff, R.A., Turney, C.S.M., van der Plicht, J., 2013. IntCal13 and Marine13 Radiocarbon Age Calibration Curves 0–50,000 Years Cal BP.

Seibold, E., 1982. The Northwest African Continental Margin — An Introduction, in: von Rad, U., Hinz, K., Sarnthein, M., Seibold, E. (Eds.), Geology of the Northwest African Continental Margin. Springer Berlin Heidelberg, Berlin, Heidelberg, pp. 3-20.

Smith, D.E., Harrison, S., Jordan, J.T., 2013. Sea level rise and submarine mass failures on open continental margins. Quaternary Science Reviews 82, 93-103.

Stuiver, M., Polach, H. A., 1977. Reporting on 14C data. Radiocarbon 19, 355–363.

Stuiver, M., Reimer, P. J., 1986. A computer program for radiocarbon age calibration. Radiocarbon 28, 1022-1030.

Sultan, N., Cochonat, P., Canals, M., Cattaneo, A., Dennielou, B., Haflidason, H., Laberg, J.S., Long, D., Mienert, J., Trincardi, F., Urgeles, R., Vorren, T.O., Wilson, C., 2004. Triggering mechanisms of slope instability processes and sediment failures on continental margins: a geotechnical approach. Marine Geology 213, 291-321.

Talling, P., Clare, M., Urlaub, M., Pope, E., Hunt, J., Watt, S., 2014. Large Submarine Landslides on Continental Slopes: Geohazards, Methane Release, and Climate Change. Oceanography 27, 32-45.

Tappin, D.R., Watts, P., McMurtry, G.M., Lafoy, Y., Matsumoto, T., 2001. The Sissano, Papua New Guinea tsunami of July 1998 — offshore evidence on the source mechanism. Marine Geology 175, 1-23.

Urgeles, R., Leynaud, D., Lastras, G., Canals, M., Mienert, J., 2006. Back-analysis and failure mechanisms of a large submarine slide on the ebro slope, NW Mediterranean. Marine Geology 226, 185-206.

Urlaub, M., Talling, P.J., Masson, D.G., 2013. Timing and frequency of large submarine landslides: implications for understanding triggers and future geohazard. Quaternary Science Reviews 72, 63-82.

Urlaub, M., Talling, P.J., Zervos, A., Masson, D., 2015. What causes large submarine landslides on low gradient (<2°) continental slopes with slow (~0.15 m/kyr) sediment accumulation? Journal of Geophysical Research: Solid Earth 120, 6722-6739.

Vanneste, M., Mienert, J., Bunz, S., 2006. The Hinlopen Slide: A giant, submarine slope failure on the northern Svalbard margin, Arctic Ocean. Earth and Planetary Science Letters 245, 373-388.

Vanneste, M., Sultan, N., Garziglia, S., Forsberg, C.F., L'Heureux, J.-S., 2014. Seafloor instabilities and sediment deformation processes: The need for integrated, multi-disciplinary investigations. Marine Geology 352, 183-214.

Varnes, D.J., 1978. Slope movement types and processes, in Schuster, R.L., and Krizek, R.J., eds., Landslides-Analysis and control: National Research Council, Washington, D.C., Transportation Research Board, Special Report 176, 11-33.

Watts, P., Grilli, S.T., Tappin, D.R., Fryer, G.J., 2005. Tsunami Generation by Submarine Mass Failure. II: Predictive Equations and Case Studies. Journal of Waterway, Port, Coastal, and Ocean Engineering 131, 298-310.

Weaver, P.P.E., Kuijpers, A., 1983. Climatic control of turbidite deposition on the Madeira Abyssal Plain. Nature 306, 360-363.

Weaver, P.P.E., Wynn, R.B., Kenyon, N.H., Evans, J., 2000. Continental margin sedimentation, with special reference to the north-east Atlantic margin. Sedimentology 47, 239-256.

Wynn, R.B., Masson, D.G., Stow, D.A.v., Weaver, P.P.E., 2000. The Northwest African slope apron: a modern analogue for deep-water systems with complex seafloor topography. Marine and Petroleum Geology 17, 253-265.

Zhao, F., Alves, T.M., Li, W., Wu, S., 2015. Recurrent slope failure enhancing source rock burial depth and seal unit competence in the Pearl River Mouth Basin, offshore South China Sea. Tectonophysics 643, 1-7.

Figure Captions

Fig. 1 Combined bathymetric and topographic map highlighting the distribution of the Sahara Slide Complex, which is marked in yellow (modified after Wynn et al., 2000; Georgiopoulou et al., 2010). Key bathymetric and structural features include the Saharan Seamounts to the west of the Sahara Slide, and the Canary Islands to the north of the study area. The red box represents the precise location of the study area. Bathymetric contours are shown as black solid lines with intervals of 1000 m.

Fig. 2 (a) Multibeam bathymetric map of the headwall of the Sahara Slide Complex. The map highlights the presence of a complex headwall and associated sidewall scarps. The black boxes show the locations of the illuminated perspective views in Fig. 3. Interpreted sidescan sonar mosaics are outlined by the blue box (see detail in Fig. 6). The black solid lines indicate the Parasound profiles used in this study (Figs. 4a, b and 5a). Contours are shown at intervals of 200 m. The red circles represent the locations of sediment cores acquired during Cruise P395. (b) Profile A-A' (see location in Fig. 2a) illustrates the locations of the upper and lower headwall; each one with a height of ~100 m.

Fig. 3 Three-dimensional (3D) perspective of the upper headwall of the Sahara Slide. See Fig. 2 for location of the 3D views. (a) Northeastern part of the upper headwall showing key morphological features including headwall scarps, glide planes (GP I, GP II and GP III) and Plateau I. (b) Southeastern part of the upper headwall showing headwall scraps, sidewall scarps and glide planes (GPI, GPII and GP III). (c) Central part of the upper headwall showing multiple sediment blocks and erosive channels.

Fig. 4 (a) Parasound profile crossing the upper headwall towards the distal part of the Sahara Slide. The zoomed section reveals stratified sediments separated by a glide plane from slide deposits above. (b) Along-slope Parasound profile crossing the upper headwall showing a sidewall scarp, and Plateaus I and II. Three different glide planes (GP I, II and III) are highlighted in the figure by a yellow dashed line. The locations of the profiles are shown in Fig. 2.

Fig. 5 (a) Parasound profile crossing the distal part of the upper headwall of the Sahara Slide Complex, along the continental slope. The profile shows well-developed sidewall scarps and numerous slide blocks. (b) Zoomed section imaging slide deposits over two distinct glide planes. The yellow dashed line highlights the position of the glide plane. (c) Zoomed section revealing the slide deposits and the underlying undulated glide plane. Location of profile is shown in Fig. 2.

Fig. 6 Sidescan sonar mosaic on the upper headwall of the Sahara Slide Complex. Dark colors represent areas of high backscatter. Four different acoustic facies, two lobes and plateau I, II are indicated in the mosaic. The white boxes highlight the zoomed sections in Figs. 8a, 9a and 10a. The inset figure shows the distribution of the three glide planes (GP I, II and III).

Fig. 7 Interpretation of the sidescan sonar data in Fig. 6 highlighting the distribution of four acoustic facies in the upper headwall of Sahara Slide Complex. See text for details.

Fig. 8 (a) Sidescan sonar data of the northern part of the upper headwall showing acoustic Facies 1 and 3a. Dark colors represent areas of high backscatter. See Fig. 6 for location of the mosaic. Multiple cracks are observed near the headwall. (b) Sub-bottom profile revealing the morphology of ridges and troughs. A high-amplitude reflection represents GP III.

Fig. 9 (a) Sidescan sonar data of the southern part of the upper headwall showing the morphology of large-scale sediment ridges. A crown crack is identified in stratified (slope) sediments south of the headwall scarp. Dark colors represent areas of high backscatter. See Fig. 6 for location of sidescan sonar mosaic. (b) Zoomed section showing the morphology of the crown crack located south of the headwall. The crown crack has a length of ~ 550 m and a width of ~50 m. (c) Sub-bottom profile illustrating ridges, troughs and the headwall of the Sahara Slide Complex.

Fig. 10 (a) Sidescan sonar data of the central part of the study area, downslope from the upper headwall, showing multiple slide blocks and striae. Prominent isolated blocks are located at the termination of the striae. Dark colors represent areas of high backscatter. See Fig. 6 for location of the image (b) Sub-bottom profile showing the striae referred to in the text, which are surrounded by blocky deposits.

Fig. 11 Photo and schematic illustration of sediment cores P395-04-1 and P395-07-1 (see Fig. 2 for location of cores). Black solid dots in core P395-04-1 and P395-07-1 represent the positions of AMS 14C-age dating samples in 5 and 3 cm below seafloor (bsf) with the calibrated ages. Note the distance from sample location to the boundary between Holocene drape and debris, which is ~1 cm for core P395-07-1.

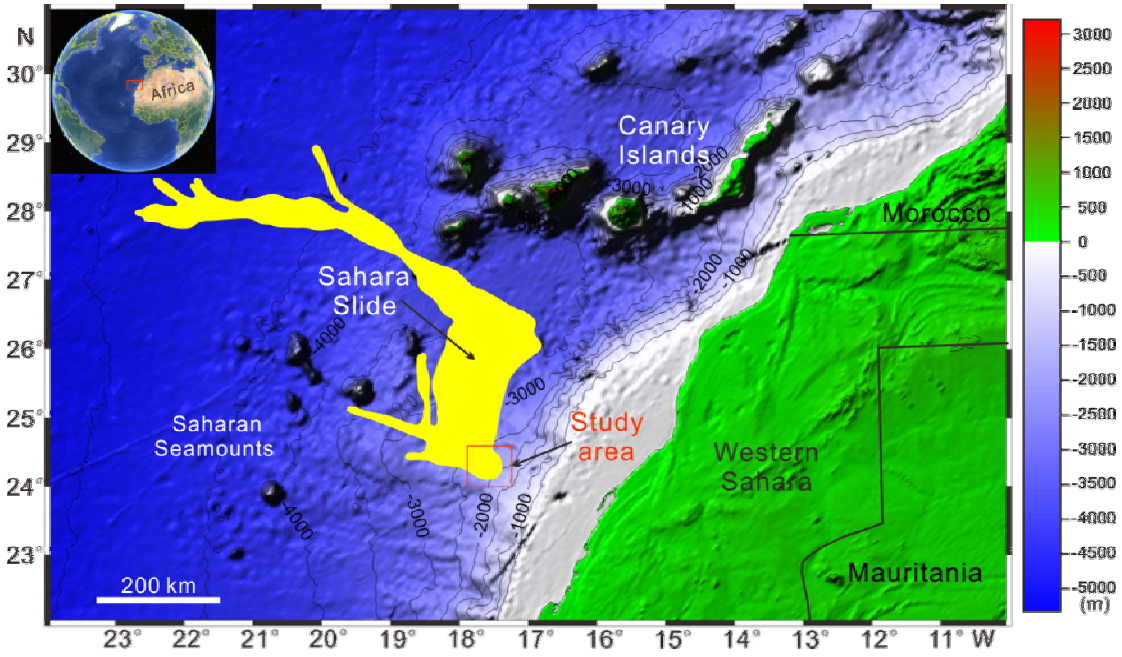
N
30°
29°
28°
27°
26°
25°
24°
23°
Africa
Canary
Islands
Morocco
Sahara
Slide
Saharan
Seamounts
Study
area
Western
Sahara
Mauritania
200 km
23° 22° 21° 20° 19° 18° 17° 16° 15° 14° 13° 12° 11° W
3000
2500
2000
1500
1000
500
0
-500
-1000
-1500
-2000
-2500
-3000
-3500
-4000
-4500
-5000
(m)

Figure 1

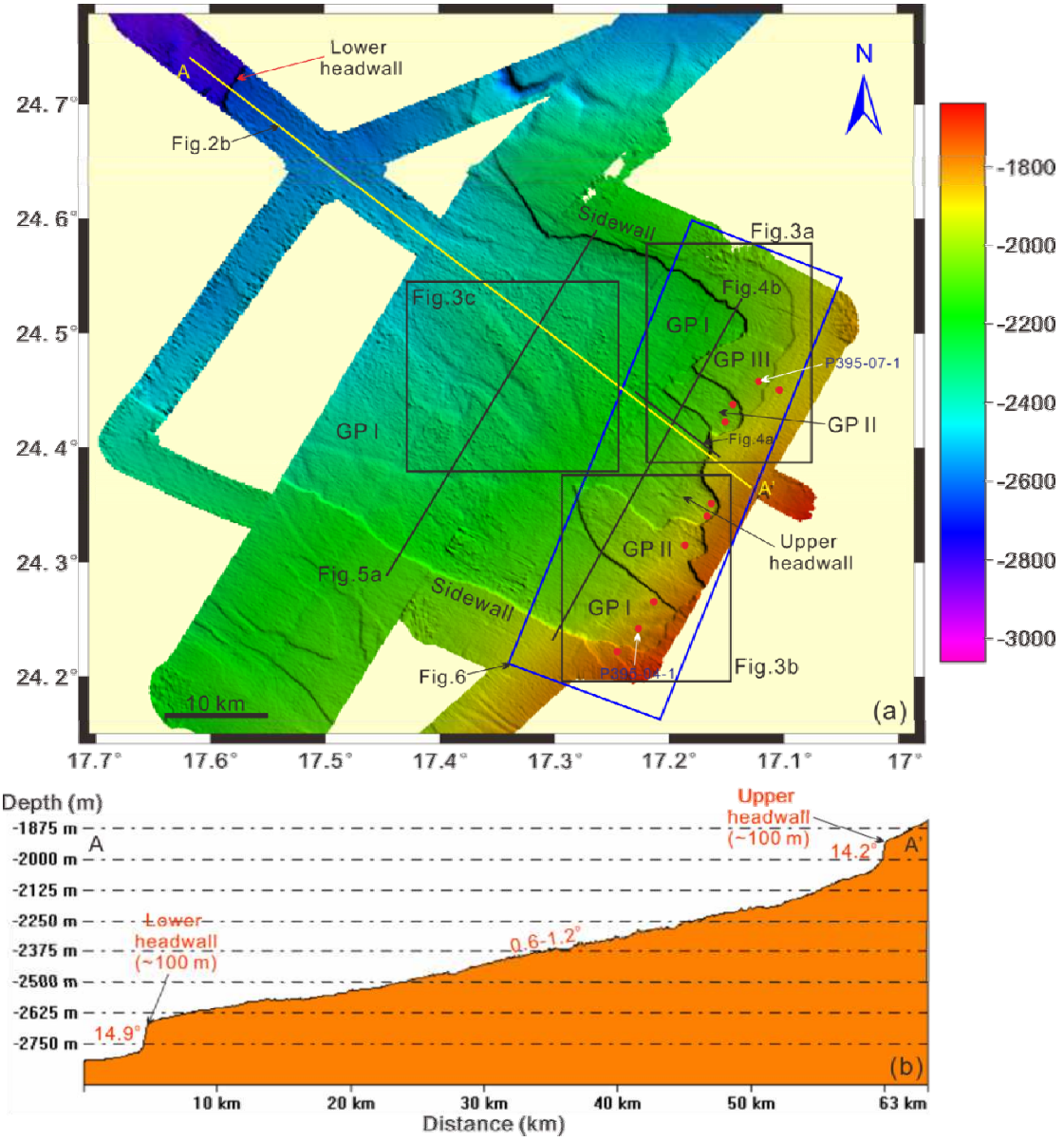
Lower headwall
A
Fig.2b
N
Sidewall
Fig.3a
Fig.4b
Fig.3c
GP I
GP III
P395-07-1
GP II
Fig.4a
GP I
A'
Upper headwall
GP II
Fig.5a
Sidewall
GP I
Fig.6
P395-04-1
Fig.3b
10 km
(a)
24.7°
24.6°
24.5°
24.4°
24.3°
24.2°
17.7°
17.6°
17.5°
17.4°
17.3°
17.2°
17.1°
17°
-1800
-2000
-2200
-2400
-2600
-2800
-3000
Depth (m)
-1875 m
-2000 m
-2125 m
-2250 m
-2375 m
-2500 m
-2625 m
-2750 m
A
Upper headwall (~100 m)
14.2°
A'
Lower headwall (~100 m)
0.6-1.2°
14.9°
(b)
10 km
20 km
30 km
40 km
50 km
63 km
Distance (km)

Figure 2

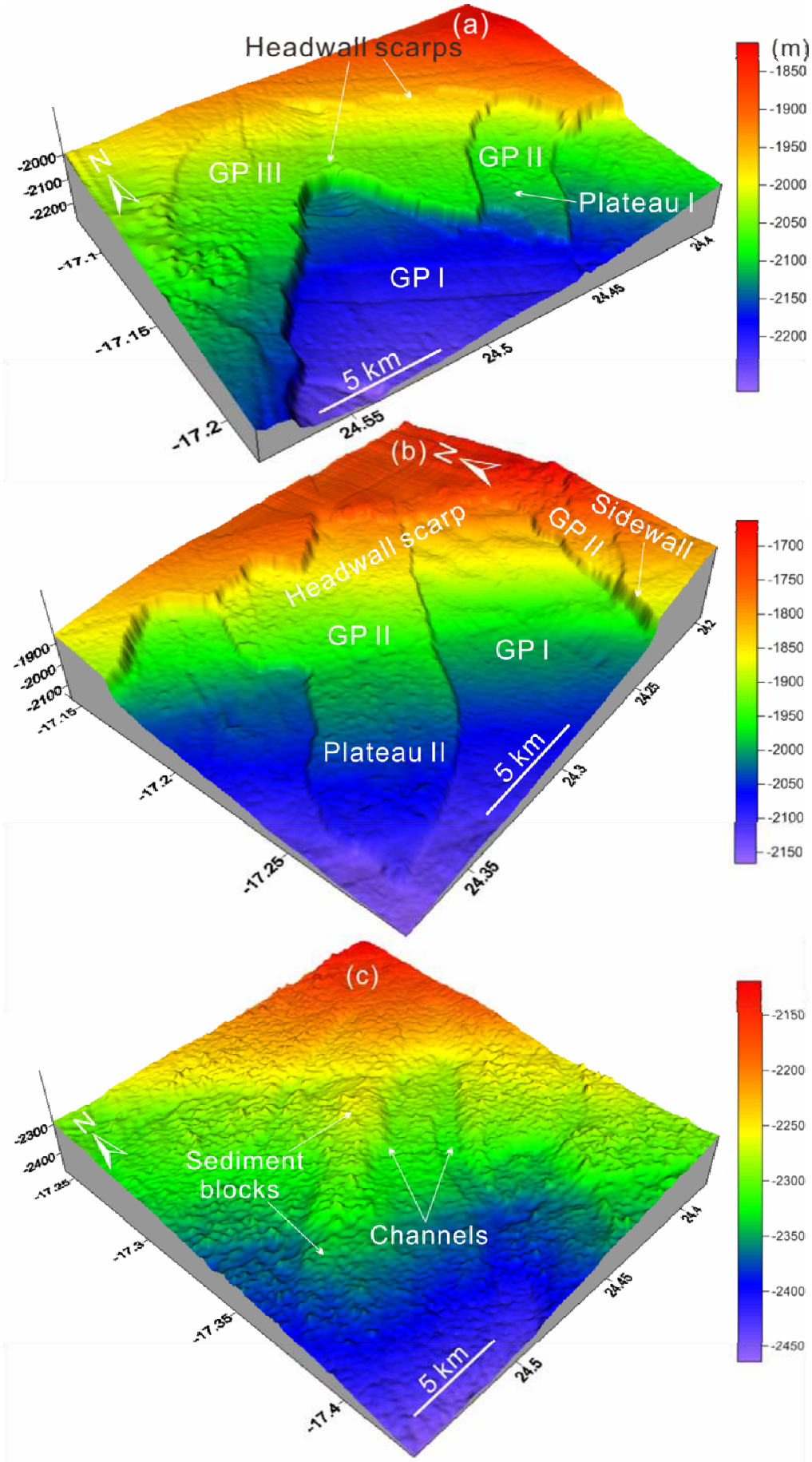
(a)
Headwall scarps
GP III
GP II
Plateau I
GP I
5 km
(m)
-1850
-1900
-1950
-2000
-2050
-2100
-2150
-2200
(b)
Headwall scarp
GP II
Sidewall
GP II
GP I
Plateau II
5 km
-1700
-1750
-1800
-1850
-1900
-1950
-2000
-2050
-2100
-2150
(c)
Sediment blocks
Channels
5 km
-2150
-2200
-2250
-2300
-2350
-2400
-2450

Figure 3

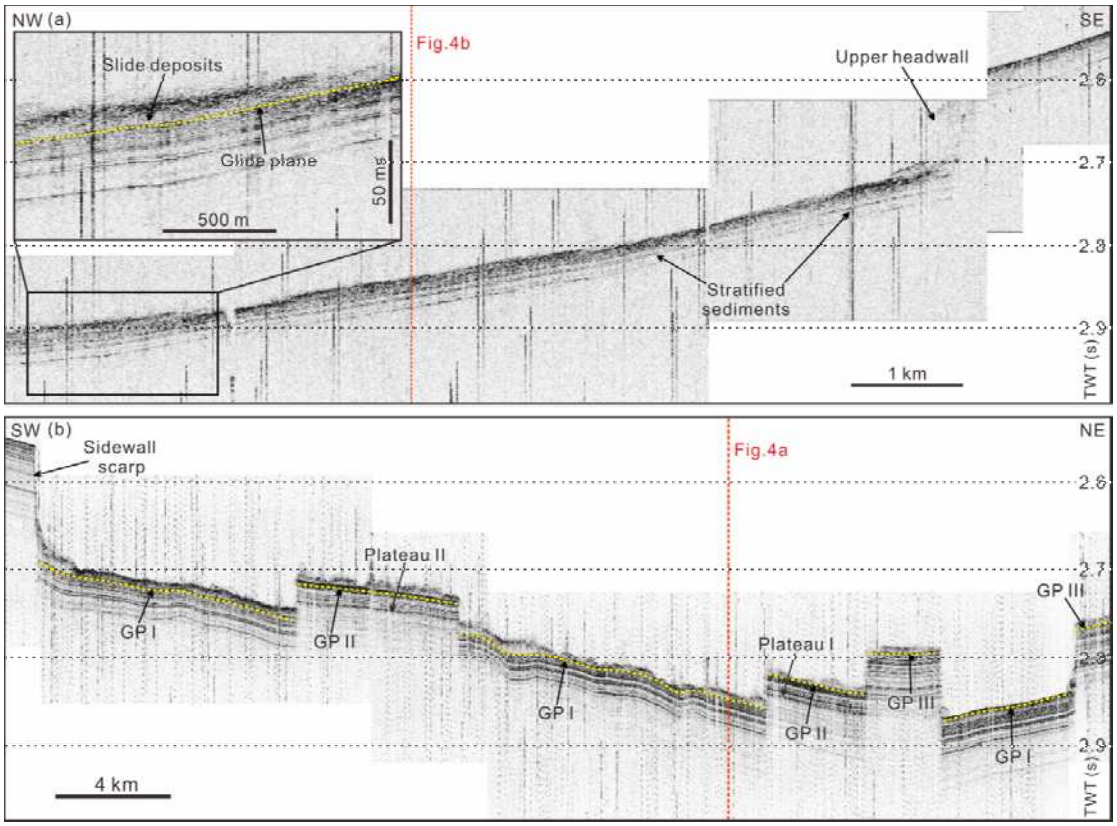

Figure 4

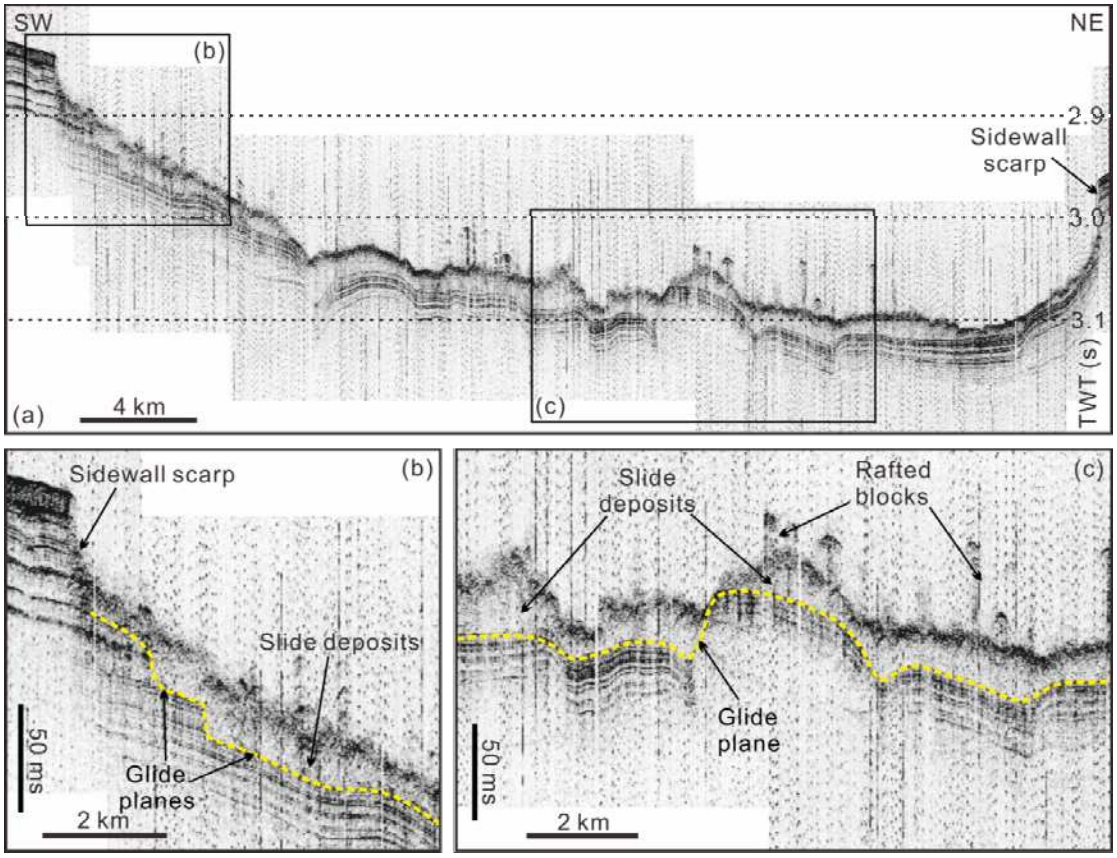

Figure 5

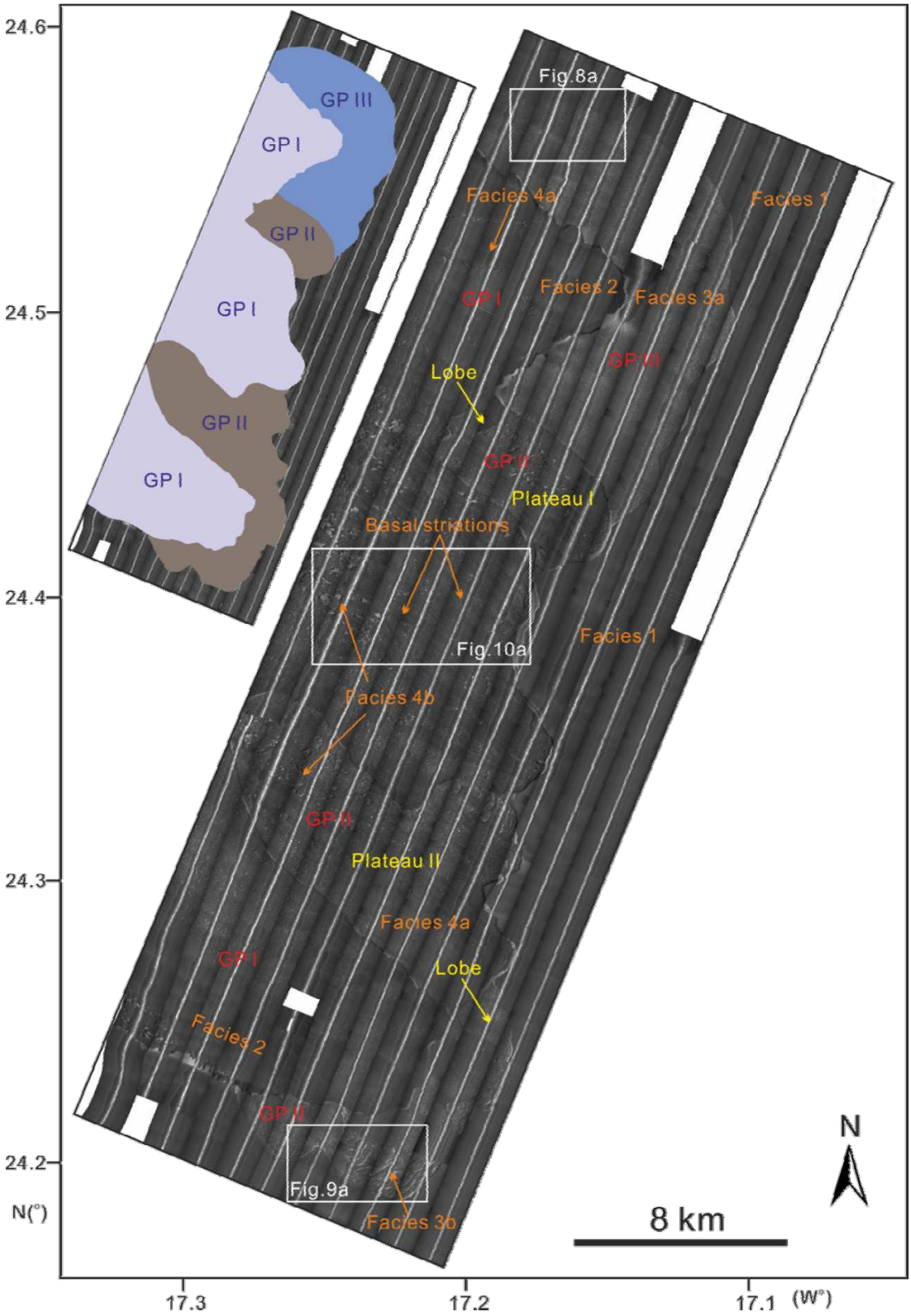
24.6
24.5
24.4
24.3
24.2
N(°)
17.3
17.2
17.1
(W°)
GP III
GP I
GP II
GP I
GP II
GP I
Fig.8a
Facies 4a
Facies 1
GP I
Facies 2
Facies 3a
GP III
Lobe
GP II
Plateau I
Basal striations
Fig.10a
Facies 1
Facies 4b
GP II
Plateau II
Facies 4a
GP I
Lobe
Facies 2
GP II
Fig.9a
Facies 3b
N
8 km

Figure 6

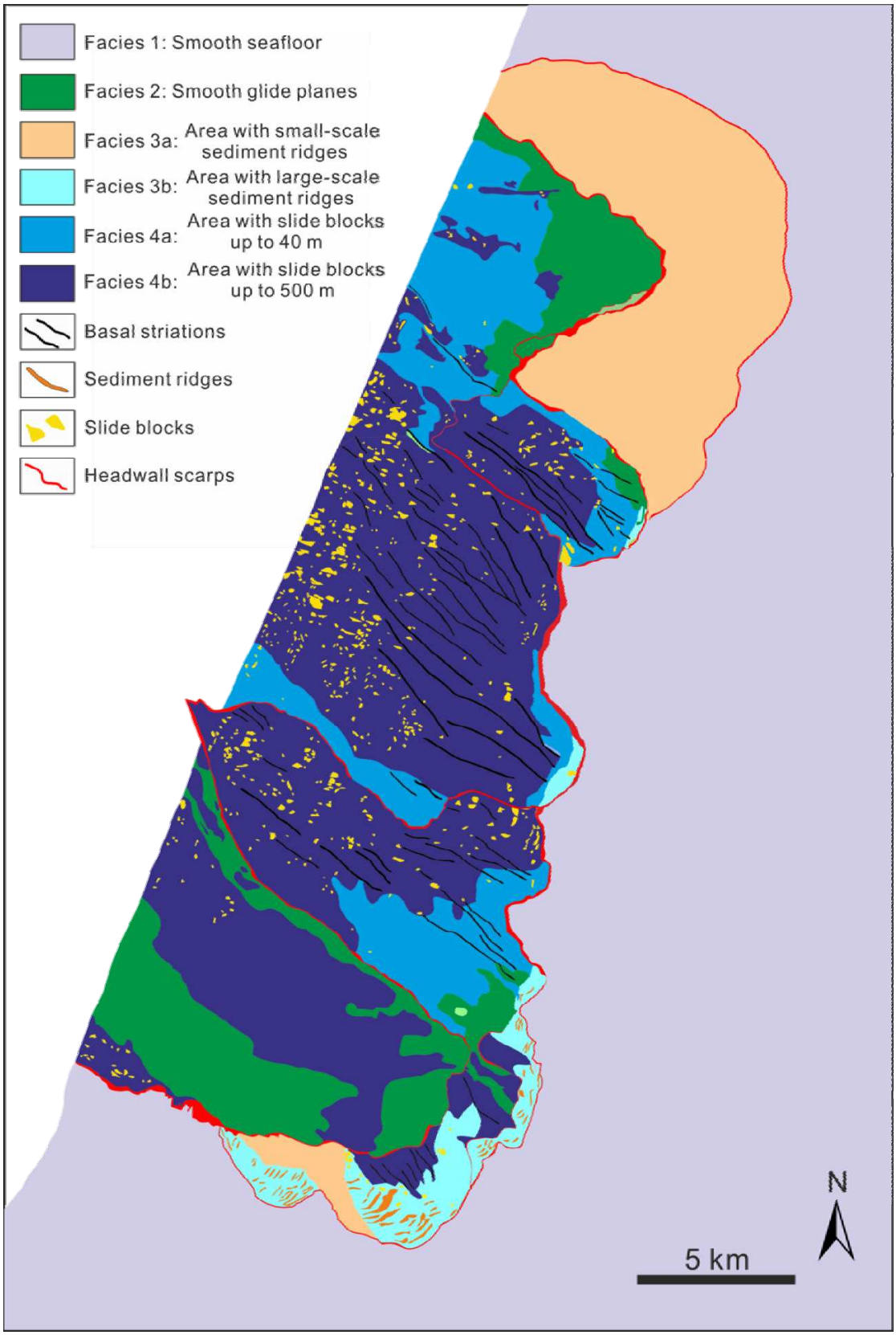
Facies 1: Smooth seafloor
Facies 2: Smooth glide planes
Facies 3a: Area with small-scale sediment ridges
Facies 3b: Area with large-scale sediment ridges
Facies 4a: Area with slide blocks up to 40 m
Facies 4b: Area with slide blocks up to 500 m
Basal striations
Sediment ridges
Slide blocks
Headwall scarps
N
5 km

Figure 7

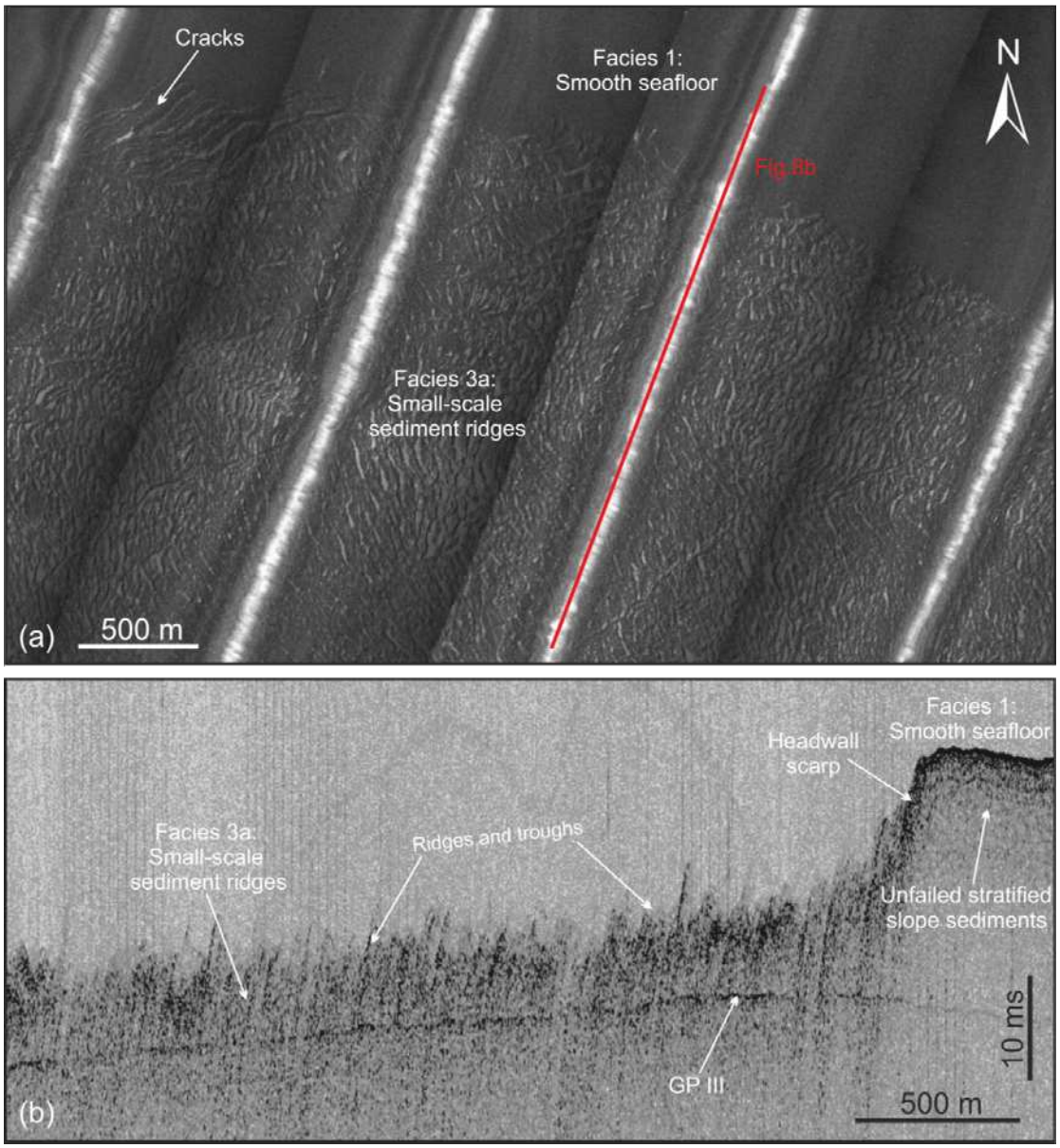
Cracks
Facies 1:
Smooth seafloor
N
Fig.8b
Facies 3a:
Small-scale
sediment ridges
(a)
500 m
Facies 1:
Smooth seafloor
Headwall
scarp
Facies 3a:
Small-scale
sediment ridges
Ridges and troughs
Unfailed stratified
slope sediments
10 ms
GP III
(b)
500 m

Figure 8

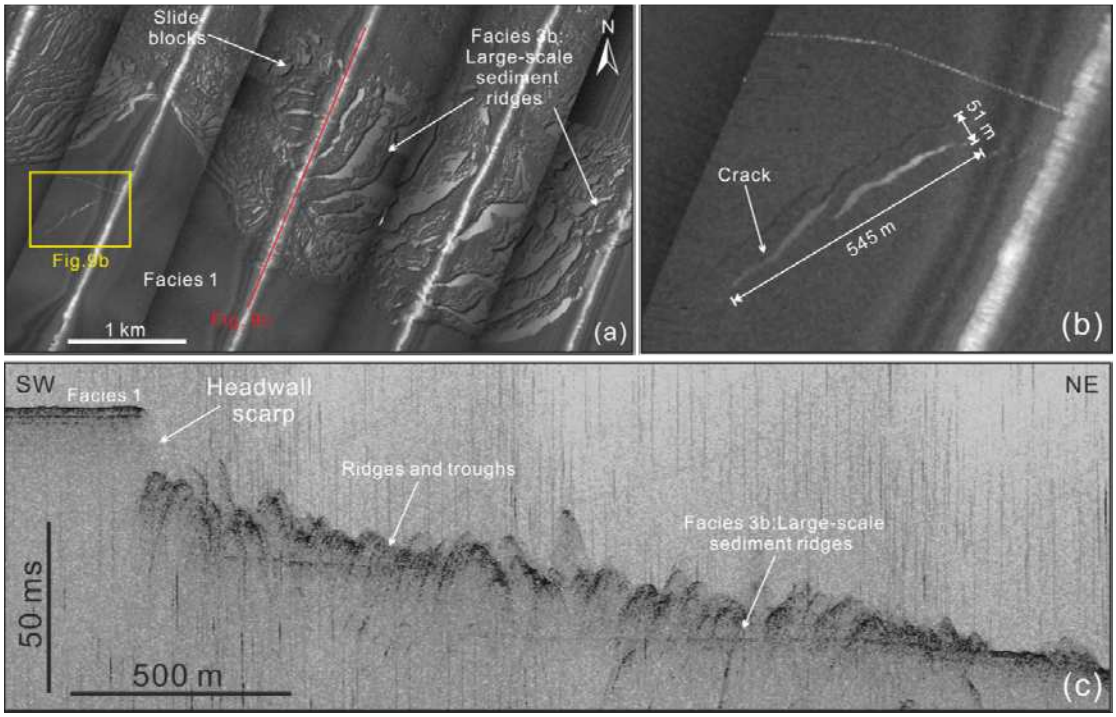
Slide blocks
Facies 3b: Large-scale sediment ridges
N
Fig.9b
Facies 1
1 km
(a)
Crack
51 m
545 m
(b)
SW
Facies 1
Headwall scarp
NE
Ridges and troughs
Facies 3b:Large-scale sediment ridges
50 ms
500 m
(c)

Figure 9

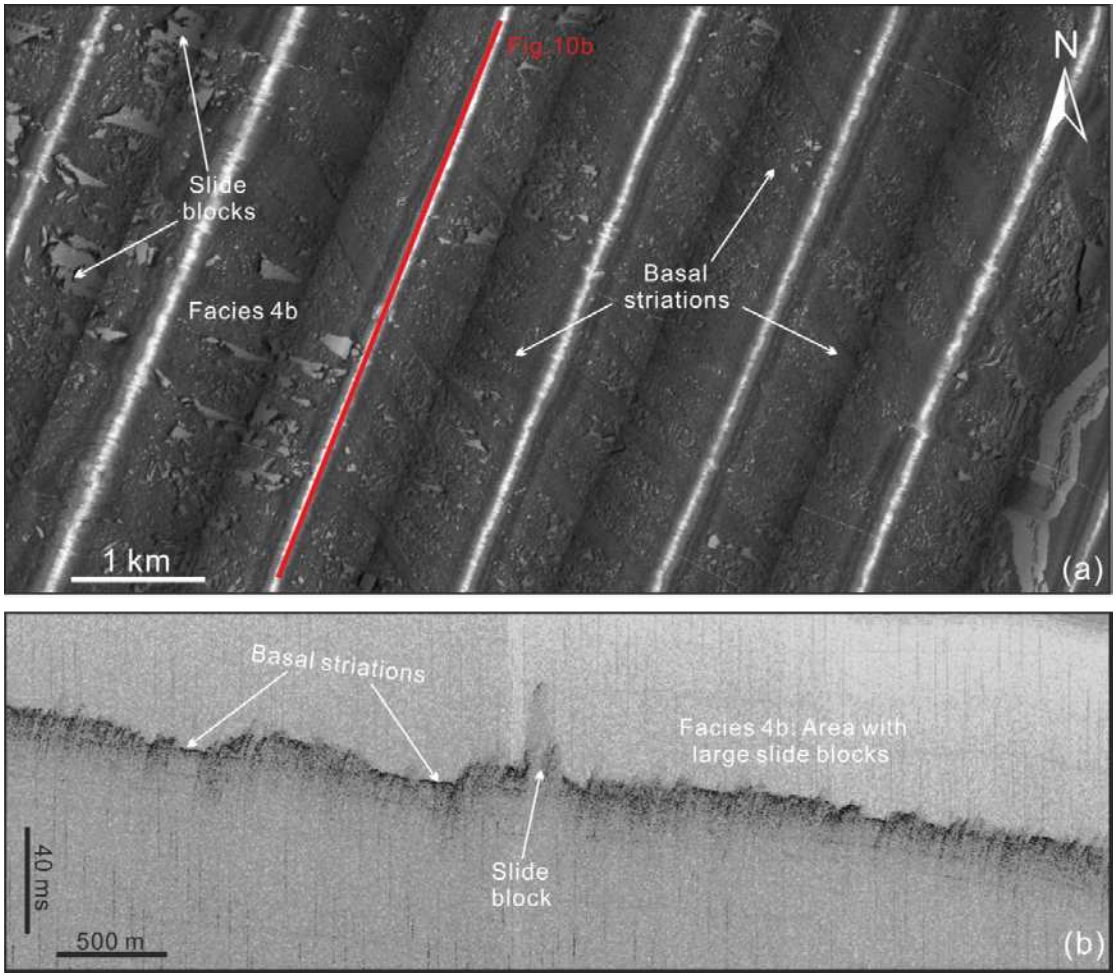
Fig.10b
N
Slide blocks
Facies 4b
Basal striations
1 km
(a)
Basal striations
Facies 4b: Area with large slide blocks
Slide block
40 ms
500 m
(b)

Figure 10

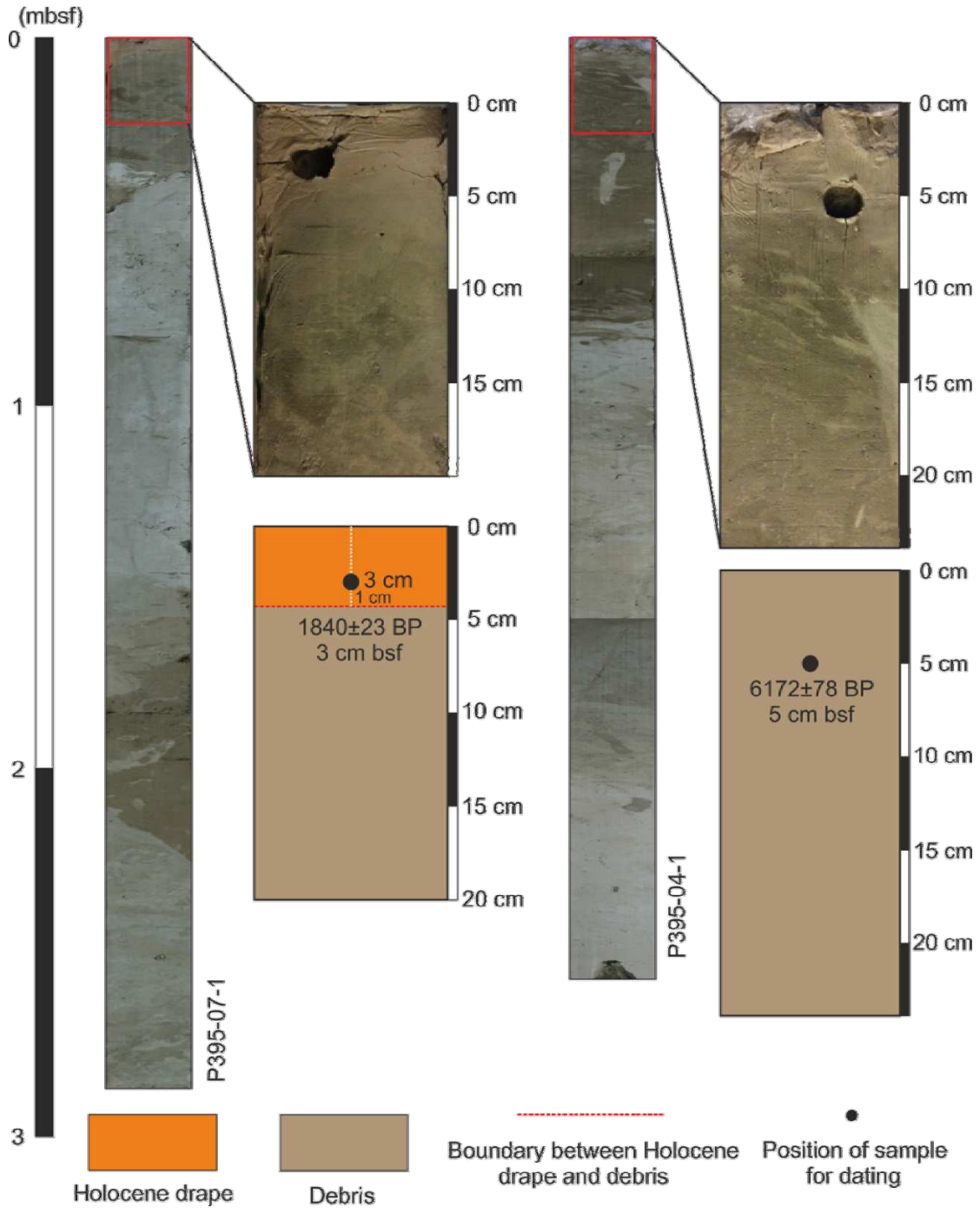

Figure 11